Finite-size effects on order reconstruction around nematic defects

Samo Kralj
Department of Physics, Faculty of Natural Sciences and Mathematics, University of Maribor, Koroška cesta 160, SI-2000 Maribor, Slovenia and Jožef Stefan Institute, P.O. Box 3000, SI-1000 Ljubljana, Slovenia

Riccardo Rosso and Epifanio G. Virga
Dipartimento di Matematica and CNISM, Università di Pavia, via Ferrata 1, I-27100 Pavia, Italy
(Received 9 July 2009; revised manuscript received 15 November 2009; published 3 February 2010)

By use of the Landau–de Gennes phenomenological theory, we study the texture of a nematic liquid crystal confined within a hybrid cell. Precisely, we consider cylindrically symmetric solutions containing topological defects dictated by appropriate boundary conditions. We focus our attention on cells whose dimensions are comparable with the biaxial correlation length ξ_b. For such severe confinements the order reconstruction (OR) configuration could be stable. Its structural details reflect the balance among boundary-enforced frustration, elastic penalties, and finite-size effects. In particular, we analyze the interplay between finite-size effects and topological defects. We show that defects are always pinned to the negatively (planar) uniaxial sheet of the OR structure. The presence of a ring defect can dramatically increase the critical threshold below which the OR structure is stable.

DOI: 10.1103/PhysRevE.81.021702 PACS number(s): 61.30.Pq, 61.30.Jf, 64.60.Q−

I. INTRODUCTION

Recent years witnessed an increasing interest for nanodevices [1,2] that can be employed, *inter alia*, as detectors sensitive at the molecular scale, nanomachines or memory elements [3] with possible applications in a broad range of different areas. Soft-matter-based devices [4] seem promising as working materials since a relatively weak local perturbation could trigger an apparent mesoscopic or even macroscopic response [5]. Such extreme responses could in particular be achieved in phases or structures reached via a continuous symmetry-breaking phase transition [6]. These systems possess collective Goldstone fluctuation modes in the symmetry-breaking continuum field which are relatively easy to excite [7].

Confined systems suffering continuous symmetry-breaking transitions almost inevitably display topological defects [4,6,8,9]. These exhibit order parameter configurations that cannot be transformed locally into the ground state configuration via continuous transformations. At the defect site, the symmetry breaking field is not uniquely defined. Defects can be treated as objects carrying a topological charge, which is a conserved quantity [10]. In a bulk system, one can get rid of defects only via mutual annihilation of their charges. The region where the presence of a defect causes apparent deviations from bulk ordering is referred to as the defect *core* [11]. Its linear dimension is roughly given by the correlation length ξ of the order parameter field employed to describe the phase transition. The defect core typically exhibits a different phase with higher energy density than that in the surrounding phase.

Simple representatives of such systems used in various applications are thermotropic uniaxial liquid crystals (LCs) [8,12] consisting of rodlike molecules exhibiting an isotropic (I) to nematic (N) phase transition at the critical temperature $T=T_{IN}$. In the isotropic phase, the molecules strongly fluctuate isotropically whereas in the nematic phase they tend to align themselves along a single symmetry-breaking direction.

Strictly speaking, this picture is valid for an unconstrained nematic LC. When it is confined in the submicrometer regime, its structural and phase behavior can significantly differ from that of bulk samples. In fact, a confined LC equilibrium configuration results from the interplay among surface interactions, elastic distortions and finite-size effects. When the confinement is particularly severe, in the presence of antagonistic, sufficiently strong uniaxial anchorings, order reconstruction (OR) [13,14] is a mechanism apt to relax surface-induced frustrations. An appropriate mathematical description of OR requires an order tensor $\mathbf{Q}$: it occurs when two eigenvalues of $\mathbf{Q}$ gradually approach each other until they coalesce without involving a rotation of the eigenframe of $\mathbf{Q}$. Two conflicting uniaxial orderings can thus be reconciled through a range of biaxial states that erect a bridging wall, whose innermost core is negatively (planar) uniaxial. OR structures have been investigated in detail [13,15–17] for various boundary conditions in nematic cells bounded by parallel walls for which the characteristic linear size of the confining plates is large—virtually infinite—compared to the cell thickness. As a result, the corresponding structures exhibit spatial variations along a single spatial coordinate. OR structures could be stable in thin enough cells [13,15,16], where the critical thickness is comparable to the biaxial order parameter length ξ_b, or when a sufficiently strong electric or magnetic field is applied [17].

Order reconstruction was actually introduced to study the fine structure of defects in [18], where it was originally named *eigenvalue exchange*. Through this mechanism, biaxial core structures arise that avoid local melting of nematic ordering. Theoretical investigations [19–23] for conventional LCs suggest that biaxial, rather than isotropic, core structures of both line and point defects are more likely to occur, particularly in the deep nematic phase. The predicted nematic core structures are so small that they have not yet been ac-

cessed experimentally: for biaxial structures, the linear size of the defect core is comparable to ξ_b, and so it is a nanoscopic length-scale. However, it has been shown that defect structures obtained from theories in the same league as Landau–de Gennes' are in good agreement with those obtained from molecular simulations, where clusters of nematic molecules are represented as Gay-Berne ellipsoids [24,25].

In this paper, we analyze the structural behavior of a relatively simple system consisting of a nematic LC confined within a cylindrically symmetric hybrid cell of thickness comparable to ξ_b. Structural features are retraced by using a mesoscopic Landau–de Gennes approach in which the nematic ordering is described in terms of a tensorial order parameter. Recent studies [26–28] reveal that mesoscopic Landau–de Gennes theories well predict structural and phase behaviors of severely confined LCs, although the thermodynamic limit is far from being reached. Here, we analyze different OR structures and show that large nonsingular elastic distortions are pinned to topological defects.

The plan of the paper is as follows. The theoretical background is presented in Sec. II where the expression of the free energy is discussed and the system is described. We use two parameterizations for the order tensor: one for computational purposes, and the other to visualize better the different examined structural variations. Appropriate dimensionless Euler-Lagrange equations are written and boundary conditions are discussed. Section III contains the main results of the paper and Sec. IV summarizes our conclusions. Technical details are deferred to two Appendices.

II. THEORETICAL BACKGROUND

A. Free energy

At the mesoscopic scale we describe the nematic ordering by a symmetric, traceless *order tensor* $\mathbf{Q}$ represented as [4]

$$\mathbf{Q} = \sum_{i=1}^{3} \lambda_i \boldsymbol{e}_i \otimes \boldsymbol{e}_i, \tag{1}$$

where $\boldsymbol{e}_i$ are orthogonal unit vectors representing the eigenvectors of $\mathbf{Q}$ and λ_i are its eigenvalues, which, to interpret $\mathbf{Q}$ as the traceless second-moment tensor of the molecular distribution function, must be such that $\lambda_i \in [-\frac{1}{3}, \frac{2}{3}]$. In this description, a nematic LC is in a uniaxial configuration when $\mathbf{Q}$ has two coincident eigenvalues and so we can write Eq. (1) as

$$\mathbf{Q} = S\left(\boldsymbol{n} \otimes \boldsymbol{n} - \frac{1}{3}\mathbf{I}\right), \tag{2}$$

where $\boldsymbol{n}$ is the nematic director field, S the uniaxial scalar order parameter, and $\mathbf{I}$ stands for the identity tensor. The unit vector $\boldsymbol{n}$ lies along the local uniaxial ordering direction. Equation (2) suggests that there is indeed no difference between $+\boldsymbol{n}$ and $-\boldsymbol{n}$, which is often referred to as the *head-to-tail* invariance. The scalar order parameter S also expresses the magnitude of fluctuations about the nematic director.

The degree of biaxiality is measured by the scalar parameter [29]

$$\beta^2 := 1 - \frac{6(\mathrm{tr}\,\mathbf{Q}^3)^2}{(\mathrm{tr}\,\mathbf{Q}^2)^3}, \tag{3}$$

ranging in the interval [0,1]. Uniaxial configurations correspond to $\beta^2=0$, while an ordering with the maximum degree of biaxiality is characterized by $\beta^2=1$. Since $\mathrm{tr}\,\mathbf{Q}=0$, and so $\mathrm{tr}\,\mathbf{Q}^3=3\det\mathbf{Q}$, the maximum value of β^2 is attained when $\mathbf{Q}$ has at least one vanishing eigenvalue.

Let a nematic LC occupy a region $\mathcal{B}$ of the three-dimensional Euclidean space, with boundary $\partial\mathcal{B}$. We express the free-energy functional $\mathcal{F}[\mathbf{Q}]$ of the nematic LC as

$$\mathcal{F}[\mathbf{Q}] := \int_{\mathcal{B}} (f_c + f_e) dV + \int_{\partial\mathcal{B}} f_s dA, \tag{4}$$

where V and A are the volume and area measures and the condensation and elastic free-energy densities, f_c and f_e, are expressed as

$$f_c := \frac{A}{2}\mathrm{tr}\,\mathbf{Q}^2 - \frac{B}{3}\mathrm{tr}\,\mathbf{Q}^3 + \frac{C}{4}(\mathrm{tr}\,\mathbf{Q}^2)^2, \tag{5}$$

$$f_e := \frac{L}{2}|\nabla\mathbf{Q}|^2, \tag{6}$$

respectively [4,8,12]. The temperature T enters the model through the coefficient $A=A_0(T-T_*)$, where T_* is the supercooling temperature of the isotropic phase, while A_0, B, and C are material constants. The elastic term f_e penalizes departures from a spatially homogeneous ordering. For simplicity, we limit attention to the one-constant approximation where the elasticity of the system is represented by a single positive elastic constant L [4,8,12]. In an unconstrained system, the bulk free energy enforces a homogeneous isotropic ordering with $S_{\mathrm{eq}}=0$, when $T>T_{IN}$, and a uniaxial nematic ordering along a symmetry-breaking director $\boldsymbol{n}$ characterized by the equilibrium value $S_{\mathrm{eq}}=\frac{B}{4C}(1+\sqrt{1-\frac{24AC}{B^2}})$, when $T<T_{IN}$.

We model the surface free-energy density f_s as [38]

$$f_s := \frac{1}{2} w\,\mathrm{tr}(\mathbf{Q}-\mathbf{Q}_s)^2, \tag{7}$$

where $w>0$ is the anchoring strength and $\mathbf{Q}_s$ describes the preferred nematic ordering at the substrate. Within this model, the strong anchoring limit is recovered when $w\to\infty$ and so it requires $\mathbf{Q}=\mathbf{Q}_s$ on $\partial\mathcal{B}$. For example, if the uniaxial orientational ordering is enforced along the unit vector $\boldsymbol{n}_s$, also called the *easy axis*, then

$$\mathbf{Q}_s = S_s\left(\boldsymbol{n}_s \otimes \boldsymbol{n}_s - \frac{1}{3}\mathbf{I}\right), \tag{8}$$

where S_s describes the surface enforced degree of uniaxial ordering, which can differ from the bulk equilibrium value S_{eq}. Other, more general anchoring energy densities have been proposed in the literature; they are briefly described in Appendix A along with an argument that shows how the simple form (7) can be considered as a good approximation to these.

The relevant material characteristic lengths [4] are the biaxial correlation length $\xi_b \propto \sqrt{L/B}$, where L is the elastic con-

stant in (6), and the surface extrapolation length $d_e \propto L/w$. Ratios of these lengths to the characteristic confinement length h determine regimes with qualitatively different behaviors. The biaxial length measures the distance over which a locally induced biaxial distortion persists in a uniaxial nematic phase. Such distortions could propagate into the whole system if $h \sim \xi_b$. The strong anchoring limit, in which the preferred surface ordering prevails, is reached for $h/d_e \gg 1$.

B. Geometry

We consider a nematic LC sample confined within a planar cell between two parallel disks of radius R, a distance h apart (see Fig. 1). We assume that the LC texture exhibits a cylindrical symmetry about the $\boldsymbol{e}_z$-axis. To describe this situation we introduce standard polar cylindric coordinates (r,ϑ,z) and the corresponding local frame $(\boldsymbol{e}_r,\boldsymbol{e}_\vartheta,\boldsymbol{e}_z)$ where $\boldsymbol{e}_r$ is the radial unit vector emanating from the symmetry axis, $\boldsymbol{e}_z$ is directed along the symmetry axis, and $\boldsymbol{e}_\vartheta := \boldsymbol{e}_z \times \boldsymbol{e}_r$. At the upper and lower plates, at $z=h$ and $z=0$, we impose uniaxial anchoring along $\boldsymbol{e}_r$ and $\boldsymbol{e}_z$, respectively. These anchoring conditions are commonly referred to as the *tangential* and *homeotropic* anchorings [4,12]. For large enough anchoring strength, such conditions enforce a surface point defect (also called a *boojum* [4,12,30]) at the center of the upper plate. The frustrating conditions at the lower plate can induce an OR structural transition in thin enough cells, that is, when $h \sim \xi_b$ [13,15,16].

In our study we consider regimes where different characteristic lengths of the system are comparable, namely, $h \sim \xi_b$, $R \sim \xi_b$, and $d_e \sim \xi_b$. We shall see below that these choices give rise to a rich structural behavior.

C. Parametrization

We assume that the order tensor $\mathbf{Q}$ can be represented as

$$\mathbf{Q}(r,z) = -2q_0 \boldsymbol{e}_\vartheta \otimes \boldsymbol{e}_\vartheta + (q_0+q_\delta)\boldsymbol{e}_r \otimes \boldsymbol{e}_r + (q_0-q_\delta)\boldsymbol{e}_z \otimes \boldsymbol{e}_z + q_m(\boldsymbol{e}_r \otimes \boldsymbol{e}_z + \boldsymbol{e}_z \otimes \boldsymbol{e}_r), \tag{9}$$

where q_0, q_δ, and q_m are functions of r and z. Hence, $\boldsymbol{e}_\vartheta$ is always an eigenvector of $\mathbf{Q}$. This choice rules out, for example, distortions that are twisted along $\boldsymbol{e}_\vartheta$. The parameter q_m in Eq. (9) reveals departures of the eigenframe $(\boldsymbol{e}_1,\boldsymbol{e}_2,\boldsymbol{e}_3)$ of $\mathbf{Q}$ from $(\boldsymbol{e}_r,\boldsymbol{e}_\vartheta,\boldsymbol{e}_z)$, the two frames being coincident when $q_m=0$. In general, the eigenvectors $(\boldsymbol{e}_1,\boldsymbol{e}_3)$ in the plane $(\boldsymbol{e}_r,\boldsymbol{e}_z)$ are rotated by an angle $\varphi \in [0,\pi)$ with respect to the pair $(\boldsymbol{e}_r,\boldsymbol{e}_z)$, so that we can write

$$\boldsymbol{e}_1 = \sin\varphi \boldsymbol{e}_r + \cos\varphi \boldsymbol{e}_z,$$

$$\boldsymbol{e}_2 = \boldsymbol{e}_\vartheta,$$

$$\boldsymbol{e}_3 = -\cos\varphi \boldsymbol{e}_r + \sin\varphi \boldsymbol{e}_z. \tag{10}$$

The parameters q are also related to the eigenvalues of $\mathbf{Q}$ through the equations $\lambda_1=-2q_0$, $\lambda_2=q_0-\rho$, and $\lambda_3=q_0+\rho$, where

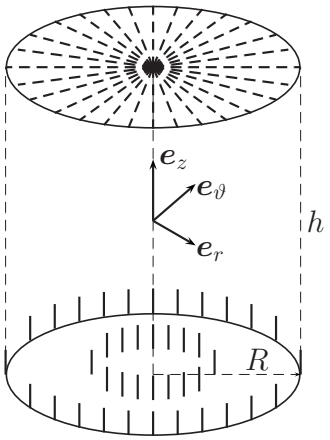

FIG. 1. Sketch of a cylindrical hybrid cell. At the lower plate the enforced ordering is homeotropic and positively uniaxial. At the upper plate, the enforced ordering is again positively uniaxial, but radial, which, for strong enough anchorings, induces a boojum at the center of the upper plate. On the lateral wall, either free boundary conditions or different uniaxial configurations are prescribed.

$$\rho := \sqrt{q_\delta^2 + q_m^2}. \tag{11}$$

The exchange of eigenvalues $\lambda_2 \leftrightarrow \lambda_3$ occurs wherever $\rho=0$ [18]. It takes place at the core of either point or line defects [31] and can be viewed as a local OR [13,15]. The assumed cylindrical symmetry of the solutions requires the parameters q involved in the representation (9) to depend only on the coordinates r and z.

To illustrate our results, in the sequel we shall need the following alternative parametrization of the eigenvalues of $\mathbf{Q}$:

$$\lambda_1 = \frac{2}{3}s\cos\psi,$$

$$\lambda_2 = -\frac{2}{3}s\cos\left(\psi - \frac{\pi}{3}\right),$$

$$\lambda_3 = -\frac{2}{3}s\cos\left(\psi + \frac{\pi}{3}\right). \tag{12}$$

By Eq. (1), we clearly have

$$s = \sqrt{\frac{3}{2}\mathrm{tr}\,\mathbf{Q}^2}, \tag{13}$$

so that $s=0$ corresponds to an isotropic, or disordered state. The degree of biaxiality β^2 can be expressed as $\beta^2=\sin^2 3\psi$, and so it is a periodic function of ψ with period $\pi/3$. Possible configurations of the system attained as ψ and s are varied for a fixed eigenframe of $\mathbf{Q}$ are depicted in Fig. 2. For example, the configurations with $\psi=0$, $\psi=2\pi/3$, and $\psi=-2\pi/3$ correspond to uniaxial states with positive scalar order parameter s and director along $\boldsymbol{e}_1$, $\boldsymbol{e}_2$, and $\boldsymbol{e}_3$, respectively. Similarly, the configurations $\psi=\pi$, $\psi=-\pi/3$, and $\psi=\pi/3$ correspond to uniaxial states with negative scalar order parameter. The degree of biaxiality attains its maximum at the angles $\psi=\pm\pi/6$, $\psi=\pm\pi/2$, and $\psi=\pm 5\pi/6$.

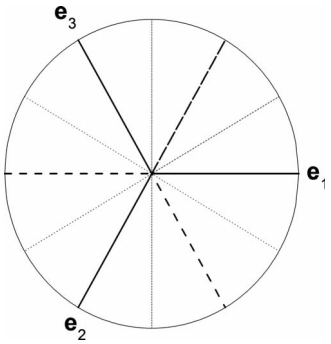

FIG. 2. Nematic states in the phase space (s,ψ). Solid lines: positively uniaxial states $(S>0)$ with $\boldsymbol{n}=\boldsymbol{e}_i$: $i=1$, $\psi=0$; $i=2$, $\psi=-\frac{2\pi}{3}$; and $i=3$, $\psi=\frac{2\pi}{3}$. Dashed lines: negatively (planar) uniaxial states $(S<0)$ with $\boldsymbol{n}=\boldsymbol{e}_i$: $i=1$, $\psi=\pi$; $i=2$, $\psi=\frac{\pi}{3}$; and $i=3$, $\psi=-\frac{\pi}{3}$. Dotted lines: states with maximal degree of biaxiality $\beta^2=1$. Along the circle, the parameter s in Eq. (13) attains its maximum value, $s=1$. At the center of the circle, $s=0$ and the phase is isotropic.

To illustrate order textures relevant to our geometric setting in the strong anchoring limit, we consider the conflicting uniaxial boundary orientations $\boldsymbol{n}(r,0)=\boldsymbol{e}_z$ and $\boldsymbol{n}(r,h)=\boldsymbol{e}_r$. We record the inner texture along a cylinder of radius r^* such that $r^*\ll R$. There are two possible ways to accommodate these conflicting boundary conditions. In one way, the eigenframe of $\mathbf{Q}$ rotates about $\boldsymbol{e}_\vartheta$ by setting for example, $\varphi(z)=\frac{z}{h}\frac{\pi}{2}$, while keeping the nematic LC in a uniaxial state. In the other way, the eigenframe of $\mathbf{Q}$ remains fixed with $\varphi=\frac{\pi}{2}$, while $\psi(z)$ varies from $\psi(0)=0$ to $\psi(h)=2\pi/3$.

We note that the representation of $\mathbf{Q}$ in terms of (φ,ψ) suffers from a drawback that makes its use in computations awkward: it is not injective. A typical transformation of (φ,ψ) that leaves $\mathbf{Q}$ unchanged, and that we need to employ when a defect is present, is [20]

$$(\varphi,\psi)\to\left(\varphi+\frac{\pi}{2},\frac{2\pi}{3}-\psi\right). \tag{14}$$

This transformation interchanges λ_1 and λ_3, it maps $\boldsymbol{e}_1$ into $\boldsymbol{e}_3$, and $\boldsymbol{e}_3$ into $-\boldsymbol{e}_1$, while leaving both λ_2 and $\boldsymbol{e}_2$ unaffected.

D. Scaling and dimensionless equilibrium equations

It is desirable to rescale appropriately the variables, so as to write dimensionless equilibrium equations. Following [15], we introduce the reduced temperature

$$\theta:=\frac{24AC}{B^2}=\frac{T-T_*}{T_{**}-T_*}, \tag{15}$$

where T_{**} is the nematic superheating temperature, and the superheating nematic order parameter

$$s_0:=\frac{B}{4C}. \tag{16}$$

In these variables, a stable homogeneous uniaxial configuration exists whenever $\theta\le\frac{T_{IN}-T_*}{T_{**}-T_*}=\frac{8}{9}$, and it is characterized by the equilibrium scalar order parameter

$$S_{eq}=s_0(1+\sqrt{1-\theta}). \tag{17}$$

Other metastable states exist, as long as $\theta\in[0,1]$. We also define the biaxial correlation length ξ_b as

$$\xi_b:=\sqrt{\frac{4LC}{B^2(\sqrt{1-\theta}+1)}}=\frac{\xi_b^{(0)}}{\sqrt{\tau}}, \tag{18}$$

where $\xi_b^{(0)}:=\frac{2\sqrt{LC}}{B}$ is the bare, temperature-independent, biaxial correlation length, and $\tau:=\sqrt{1-\theta}+1$. For conventional nematics, $\xi_b\sim 20$ nm. Accordingly, we also introduce the surface extrapolation lengths

$$d_e^{(i)}:=L/w^{(i)}, \tag{19}$$

where the superscript $i=0,1$ refers to either the lower or the upper plate, respectively.

If we rescale $\mathbf{Q}$ to s_0 and all lengths to h, we obtain the following rescaled free-energy functional:

$$\frac{32C^3}{\pi B^4h^3}\mathcal{F}[\mathbf{Q}]=\int_0^1 dz\int_0^R r[f_e+f_c]dr+\sum_{i=0}^{1}\int_0^R rf_s^{(i)}dr, \tag{20}$$

where all dimensionless quantities retain the same name as the original, dimensional variables, to avoid clutter. More precisely, in Eq. (20),

$$f_c=\frac{\theta}{6}(q_m^2+q_\delta^2+3q_0^2)-2q_0(q_m^2+q_\delta^2-q_0^2)+\frac{1}{4}(q_m^2+q_\delta^2+3q_0^2)^2, \tag{21}$$

$$f_e=\left(\frac{\xi_b^{(0)}}{h}\right)^2\left[3|\nabla q_0|^2+|\nabla q_\delta|^2+|\nabla q_m|^2+\frac{(3q_0+q_\delta)^2+q_m^2}{r^2}\right], \tag{22}$$

$$f_s^{(i)}:=\frac{(\xi_b^{(0)})^2}{2hd_e^{(i)}}\mathrm{tr}(\mathbf{Q}-\mathbf{Q}_s^{(i)})^2, \tag{23}$$

where the gradient ∇ is now intended in the dimensionless space variables, and $\mathbf{Q}_s^{(i)}$ is the preferred order tensor at the plate indexed by i.

At the lower plate $(i=0)$, we impose a strong uniaxial homeotropic anchoring, that is, we set $\mathbf{Q}_s^{(0)}=\tau(\boldsymbol{e}_z\otimes\boldsymbol{e}_z-\frac{1}{3}\mathbf{I})$, where use of Eq. (17) has also been made, and consider the limit $d_e^{(0)}\gg 1$. At the upper plate $(i=1)$ we allow a finite anchoring strength to favor the radial uniaxial configuration, that is, $\mathbf{Q}_s^{(1)}=\tau(\boldsymbol{e}_r\otimes\boldsymbol{e}_r-\frac{1}{3}\mathbf{I})$. Consequently,

$$f_s(r,0)=\frac{(\xi_b^{(0)})^2}{hd_e^{(0)}}\left[\frac{1}{3}\tau^2-q_0(\tau-3q_0)+q_\delta(q_\delta+\tau)+q_m^2\right], \tag{24}$$

$$f_s(r,1)=\frac{(\xi_b^{(0)})^2}{hd_e^{(1)}}\left[\frac{1}{3}\tau^2-q_0(\tau-3q_0)+q_\delta(q_\delta-\tau)+q_m^2\right], \tag{25}$$

with $d_{(e)}^0$ sufficiently large. At the cell's lateral boundary, $r=R$, we impose either free boundary conditions [$BC^{(free)}$] or positive uniaxial alignments. In this latter case, we either choose a uniform alignment along the z axis, by which we enforce a ring defect residing at the rim of the upper plate [$BC^{(rim)}$], or a progressive rotation of the nematic director field along $\boldsymbol{e}_z$, so as to reconcile the conflicting boundary conditions [$BC^{(rot)}$]. For a nematic LC with a positive field anisotropy, $BC^{(rim)}$ could be experimentally realized by applying in the region $r\geq R$ a strong enough electric field along the z axis [12]. We also consider $BC^{(rot)}$ to mimic the order texture that is likely to arise in a number of atomic force measurements (AFM) [32], which could be used to probe OR structures in nematics. Our setup mimics the situation in which a spherical AFM tip enforces tangential anchoring at the upper plate and its radius of curvature is so large relative to the thickness h that the tip can effectively be approximated as a plane. In such an ideal setup, the AFM apparatus should enforce homeotropic anchoring at the lower plate.

Minimization of the free energy yields the following bulk Euler-Lagrange equations for $q_0(r,z)$, $q_\delta(r,z)$, and $q_m(r,z)$ (details are given in Appendix B)

$$\left(\frac{\xi_b^{(0)}}{h}\right)^2\left(\Delta q_0-\frac{3q_0+q_\delta}{r^2}\right)-\frac{\theta}{6}q_0+\frac{1}{3}(q_\delta^2+q_m^2-3q_0^2)$$
$$-\frac{q_0}{2}(3q_0^2+q_\delta^2+q_m^2)=0, \tag{26}$$

$$\left(\frac{\xi_b^{(0)}}{h}\right)^2\left(\Delta q_\delta-\frac{3q_0+q_\delta}{r^2}\right)-\frac{\theta}{6}q_\delta+2q_0q_\delta-\frac{q_\delta}{2}(3q_0^2+q_\delta^2+q_m^2)$$
$$=0, \tag{27}$$

$$\left(\frac{\xi_b^{(0)}}{h}\right)^2\left(\Delta q_m-\frac{q_m}{r^2}\right)-\frac{\theta}{6}q_m+2q_0q_m-\frac{q_m}{2}(3q_0^2+q_\delta^2+q_m^2)=0, \tag{28}$$

where $\Delta:=\frac{\partial^2}{\partial r^2}+\frac{1}{r}\frac{\partial}{\partial r}+\frac{\partial^2}{\partial z^2}$ is the Laplace operator in polar cylindric coordinates.

At the upper plate, the weak tangential anchoring condition entails the equations

$$d_e^{(1)}q_{0,z}+q_0=\frac{\tau}{6}, \tag{29}$$

$$d_e^{(1)}q_{\delta,z}+q_\delta=\frac{\tau}{2}, \tag{30}$$

$$d_e^{(1)}q_{m,z}+q_m=0. \tag{31}$$

Here and in the following, a comma denotes differentiation with respect to a space variable. At the lower plate ($z=0$) we enforce an infinitely strong uniaxial homeotropic anchoring, corresponding to the limit when $d_e^{(0)}\to 0$ and Eq. (24) is replaced by

$$q_0=\frac{\tau}{6},\quad q_m=0,\quad q_\delta=-3q_0=-\frac{\tau}{2}. \tag{32}$$

At the lateral boundary, $r=R$, we impose either the free boundary condition $BC^{(free)}$, resulting in the equations

$$q_{0,r}=q_{m,r}=q_{\delta,r}=0, \tag{33}$$

or the positive uniaxial ordering described by

$$q_0=\frac{\tau}{6},\quad q_m=\frac{\tau}{2}\sin 2\varphi,\quad q_\delta=\frac{\tau}{2}\cos 2\varphi. \tag{34}$$

Moreover, we set $\varphi(R,z)\equiv 0$ for $BC^{(rim)}$ and $\varphi(R,z)=\frac{\pi}{2}z$ for $BC^{(rot)}$.

To prevent the integral in Eq. (20) from diverging as a consequence of f_e in Eq. (22) being singular at $r=0$, we require that there

$$q_\delta=-3q_0\quad\text{and}\quad q_m=0, \tag{35}$$

which, by Eq. (9), amounts to prescribe $\mathbf{Q}$ to be uniaxial. The cylindrical symmetry about the z axis implies that

$$q_{0,r}(0,z)=q_{\delta,r}(0,z)=q_{m,r}(0,z)=0. \tag{36}$$

Equations (26)–(28) are solved by standard relaxation methods [33], which have often been used to study LC textures in the presence of topological defects [20,34,35]. These methods retrieve the solutions to the equations of the static theory from an initial configuration of order by mimicking a dynamical process along which the total free energy is decreased. In a process of this sort, the nematic ordering could easily be trapped in a local minimum of the free-energy functional: several attempts are needed to ensure that the static configuration arrived at is indeed the one where the free-energy functional attains its absolute minimum. In the computations illustrated in the following section we repeatedly applied this sanity strategy. Moreover, especially when defects structures are found with this method, one should also ensure that it could also be reached through an ideal quenching from the isotropic, completely disordered state. This was also checked by including the disordered state $\mathbf{Q}=\mathbf{0}$ in the list of textures whence the relaxation process began. It should be noted, however, that the axial symmetry embodied in the equilibrium equations above prevents more elaborate defect textures from arising, even temporarily, during relaxation. In this respect, the question of how the defect texture we envisage here can indeed emerge from quenching remains unanswered.

III. NUMERICAL OUTCOMES

We analyze qualitatively different equilibrium textures within the cell when either h or R is $O(\xi_b)$. The equilibrium configurations mirror the interplay between elastic and surface forces, and are severely affected by the degree of confinement. Special attention is paid to interactions between regions where the presence of topological defects enhances

elastic distortions. Here we consider the main sources of elastic distortions within the cell, under different circumstances. They are first analyzed in the limit where $R \gg h$, so that different distorting sources may have a negligible mutual influence. We then examine the core structure of a typical isolated boojum which is imposed topologically at $r=0$, when $h/\xi_b \gg 1$. Finally, we study cells with $R \sim h$, where different sources of elastic distortions are bound to interact strongly.

A. Order reconstruction

In large cells ($R \gg h$) structural variations in the equilibrium solutions mainly occur along the z axis. Significant departures from this behavior are restricted to the region surrounding the symmetry axis $r=0$ by the presence of a boojum induced topologically on the upper plate, or close to the rim $r=R$ when the imposed boundary conditions are $\mathrm{BC}^{(\mathrm{rim})}$.

Averaged characteristics of OR in large cells are almost identical to those of the OR occurring in a classical hybrid cell, which is hereafter referred to as $\mathrm{OR}^{(\mathrm{cl})}$, for brevity. In this latter case, the bounding surfaces impose homogeneous competing alignments. The resulting nematic configurations exhibit spatial variations only along the z axis. In our setting, a similar structure exists far from both the cell's symmetry axis and its boundary. Structural characteristics of $\mathrm{OR}^{(\mathrm{cl})}$ have already been studied in detail in the strong anchoring limit by Palffy-Muhoray *et al.* [13] and by Bisi *et al.* [15,16]. They considered frustrated cells where either a pure bend or a pure twist elastic distortion is imposed. In fact, in the one-constant approximation, these cases are equivalent from the mathematical point of view. In such cells there are two competing equilibrium solutions, one exhibiting an essentially uniaxial structure and the other characterized by the $\mathrm{OR}^{(\mathrm{cl})}$ texture. In the strong anchoring limit their properties are as follows. The uniaxial structure is stable in thick enough cells, that is, for $h > h_c^{(\mathrm{cl})}$, where $h_c^{(\mathrm{cl})} \approx 5\xi_b$ [16]. For $h < h_c^{(\mathrm{cl})}$, the equilibrium $\mathrm{OR}^{(\mathrm{cl})}$ texture, which exists for all values of h, becomes stable. Typical structural variations are shown in Fig. 3. For $h \gg h_c^{(\mathrm{cl})}$ ($h/\xi_b=10$ in Fig. 3), the energy minimizer is essentially uniaxial, as it displays weak spatial variations in both S and β^2. Hence, the nematic configuration is well described by $S \approx S_{\mathrm{eq}}$ and $\beta^2 \approx 0$, with a director field $\boldsymbol{n}=\sin\varphi \boldsymbol{e}_r+\cos\varphi \boldsymbol{e}_z$, where $\varphi(z) \approx z\frac{\pi}{2}$. In the parametrization (9), this texture is given by

$$q_0=\frac{\tau}{6}, \quad q_m=\frac{\tau}{2}\sin 2\varphi, \quad q_\delta=-\frac{\tau}{2}\cos 2\varphi. \tag{37}$$

For smaller values of h ($h/\xi_b=5$ in Fig. 3), the degree of biaxiality within the essentially uniaxial structure progressively increases until $h=h_c^{(\mathrm{cl})}$, where the equilibrium textures loses completely its uniaxial character. For $h < h_c^{(\mathrm{cl})}$ no equilibrium uniaxial texture survives, while the $\mathrm{OR}^{(\mathrm{cl})}$ texture becomes stable. Here, the eigenframe of $\mathbf{Q}$ remains the same throughout the cell, and so $q_m \equiv 0$. Consequently, sufficiently away from the symmetry axis at $r=0$, strong variations in biaxial ordering are only displayed along z. Typical graphs of s, β^2, and ρ, as defined in Eqs. (13), (3), and (11) are shown in Fig. 4 against z for $h/\xi_b=4$. In this configuration β^2 exhibits a double-peak profile, where it attains both its maximum $\beta^2=1$ and its minimum $\beta^2=0$. This latter corresponds in real space to a sheet with negative uniaxial order along $\boldsymbol{e}_\vartheta$, as witnessed by the vanishing of ρ, see Eqs. (11) and (9). In the limit of strong anchoring on both plates, this negatively uniaxial sheet is placed at $z=h/2$.

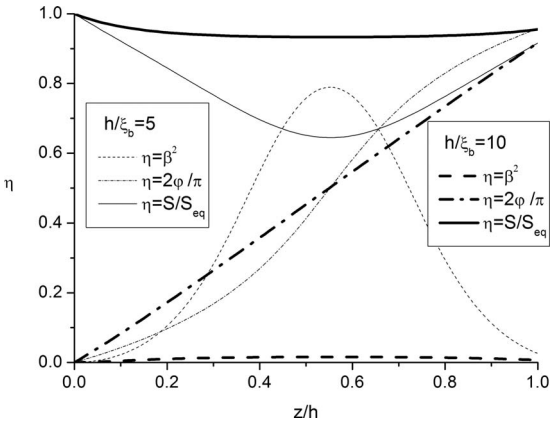

FIG. 3. Structural variations in the essentially uniaxial configuration: η stands for either $\frac{\varphi}{\pi/2}$ (dash-dotted lines), β^2 (dashed lines), or $\frac{S}{S_{\mathrm{eq}}}$ (solid lines). Here $\theta=-8$, $h/d_e^{(0)}=100$, $h/d_e^{(1)}=10$. The ratio h/ξ_b is set equal to 10 (thick lines) or to 5 (thin lines).

In Fig. 5, we plot the averaged degree of biaxiality $\langle\beta^2\rangle := \frac{1}{h}\int_0^h \beta^2(z)dz$ as a function of h/ξ_b; the plot clearly reveals a structural transition. Here, for $\theta=-8$ and in the limit of strong anchoring on both plates, the transition occurs at $h \approx 4.9\xi_b$, in agreement with the results obtained in [16] for a twist hybrid cell.

B. Boojum

We now consider the core structure of an isolated boojum enforced at $r=0$ by the boundary condition at the upper plate. The defect exists only for strong enough anchorings ($h/d_e^{(1)} > 5$) and its structure is not affected by the geometri-

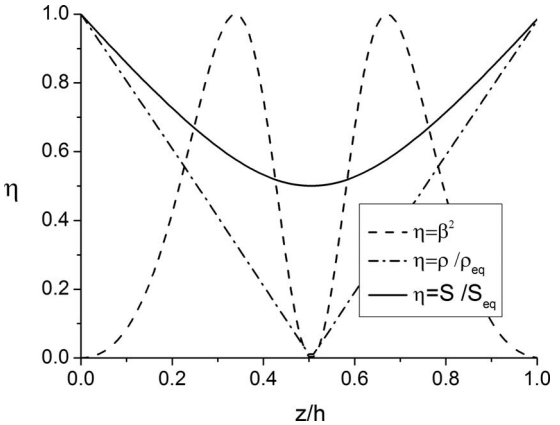

FIG. 4. Typical graphs of $s(z)$, $\beta^2(z)$, and $\rho(z)$ away from the axis $r=0$ for $\theta=-8$, and $h/\xi_b=4$ in the limit of strong anchoring on both plates. Here $\eta=\rho/\rho_{\mathrm{eq}}$ (dash-dotted line), where ρ_{eq} is the equilibrium value of ρ, $\eta=\beta^2$ (dashed line), and $\eta=S/S_{eq}$ (solid line).

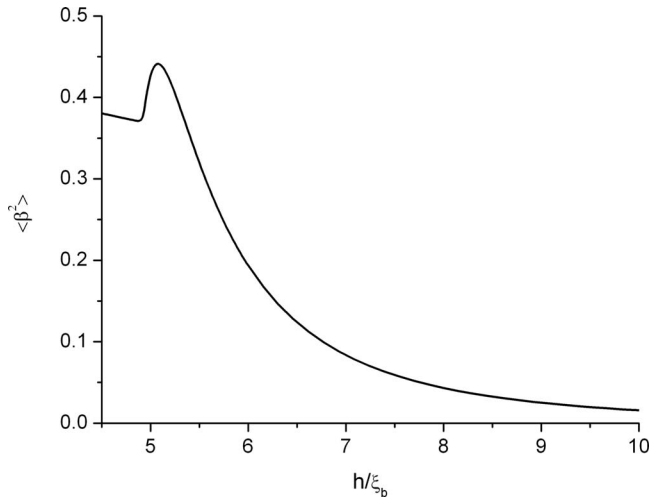

FIG. 5. The averaged degree of biaxiality $\langle\beta^2\rangle := \frac{1}{h}\int_0^h \beta^2 dz$ as a function of h/ξ_b for the $OR^{(cl)}$ texture. The structural transition occurs at $h_c/\xi_b \approx 4.9$, sufficiently away from the symmetry axis $r=0$.

cal details of the problem, provided that $h/\xi_b \gg 1$, as discussed in [30]. Its structure differs qualitatively from the core of half a hedgehog. We summarize here the main features of this defect, referring the interested reader to [30] for details.

As already discussed above, at the symmetry axis $r=0$ all equilibrium textures must be uniaxial along $\boldsymbol{e}_z$, which, by Eq. (9), requires $3q_0=-q_\delta$ and $q_m=0$. Similarly, the upper surface imposes uniaxial states, and so β^2 vanishes both on it and along the symmetry axis. The defect core is thus characterized by a uniaxial *finger* protruding into the cell's interior along its symmetry axis. This is shown in Fig. 6, where we plot the degree of biaxiality β^2 that surrounds the defect for a value of the anchoring strength at the upper plate that makes the finger sufficiently pronounced. We refer to such a core structure as the *fingered* boojum. In Fig. 7, we show cross sections of the graphs of $\varphi(r,z)$, $s(r,z)$, and $\beta^2(r,z)$, for fixed values of either r [left pannel: (a), (c), and (e)] or z [right pannel: (b), (d), and (f)]. The finger is negatively uniaxial ($S<0$). It ends in a *tip*, an isotropic point ($S=0$) at a distance $\xi_f \sim \xi_b$ from the upper surface [see Fig. 7(c)]. Below the tip, the nematic texture is positively uniaxial ($S>0$) along the axis $r=0$. The finger is embraced by a biaxial shell with $\beta^2=1$, which joins the finger's tip to the upper surface (see Figs. 6 and 7). The order parameter s defined in Eq. (13) vanishes only at the finger tip for a finite value of w [Fig. 7(c)].

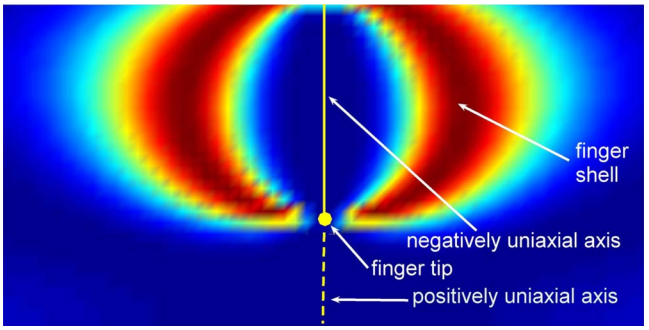

FIG. 6. (Color online) Cross-section orthogonal to the surface hosting the boojum, showing a color plot of the degree of biaxiality β^2. A biaxial shell joins the isotropic finger tip and the upper surface. The negatively (planar) uniaxial finger is the thick solid line along the symmetry axis. Along the yellow lines (white, in print), $\beta^2 \approx 0.6$; along the dark blue lines (black, in print), $\beta^2 \approx 0$; along the dark red lines (light gray, in print), $\beta^2 \approx 1$.

C. Interaction between the boojum and the uniaxial sheet

We now analyze textures resulting form allowing h and R to be comparable, so that the interaction between a defect core and the negatively uniaxial sheet of the OR structure plays a significant role. To this purpose, we consider values of h and R that are still larger than, but comparable to ξ_b. We recall that, according to recent experimental studies [26–28], nematic structures are surprisingly well described within the mesoscopic approach we use here, also at such small length-scales.

We first consider textures arising when strong anchoring is imposed at both plates and $h<h_c$, so that an OR structure prevails. A representative structure for $R/h>1$ induced by the free boundary condition $BC^{(free)}$ is shown in Fig. 8(a). We refer to the resulting configuration as the $OR^{(free)}$ texture, where the superscript refers to the type of boundary condition. We draw level curves for $\beta^2(r,z)$ in dark blue where the nematic state is essentially uniaxial and in red where the nematic state is strongly biaxial. For $R/h \gtrsim 1$ the equilibrium texture almost coincides with the $OR^{(cl)}$ structure and it is characterized by a negatively (planar) *uniaxial sheet* in the middle of the cell. The structure of the boojum residing at $r=0$ is slightly affected by the OR structure extending itself for $r>0$. On the other hand, the boojum strongly influences the OR profile near $r=0$. The uniaxial sheet is anchored at the tip of the boojum finger and then approaches the mid plane $z=h/2$ as r increases, as shown in Fig. 8. When R is small enough, the whole uniaxial sheet could be appreciably lifted above the mid plane, as shown in Fig. 8(b). Moreover, if we impose a strong uniaxial ordering along the symmetry axis, by setting $\mathbf{Q}(0,z)=\tau(\boldsymbol{e}_z\otimes\boldsymbol{e}_z-\frac{1}{3}\mathbf{I})$, with $\tau>0$, the finger is moved toward the upper plate of the cell and, for cells with $R>h$, the uniaxial sheet then rigidly follows the finger (see Fig. 8(c)). This scenario could be tested experimentally by applying locally a strong enough electric field along the z direction for a nematic LC with positive dielectric anisotropy. Some cross-sections of the graph of β^2 at fixed values of either z or r are plotted in Fig. 9. Correspondingly, Fig. 10 shows the trajectories that represent the solutions in the (s,ψ) space introduced through Eq. (12).

In Fig. 11, we illustrate the influence of the anchoring strength on the existence of OR. For any r^* sufficiently large, there are three values of z, denoted by $z_{max}^{(1)}$, z_{min}, and $z_{max}^{(2)}$, and characterized by being $\beta^2(r^*,z_{max}^{(1)})=1$, $\beta^2(r^*,z_{min})=0$, and $\beta^2(r^*,z_{max}^{(2)})=1$. In the strong anchoring limit for both plates, $0<z_{max}^{(1)}<z_{min}<z_{max}^{(2)}<1$. We then retrace the values of $z_{max}^{(1)}$, z_{min}, and $z_{max}^{(2)}$ at $r=R/2$, when the anchoring strength at the upper plate is decreased. It turns out that, upon decreasing the anchoring strength, elastic distortions gradually

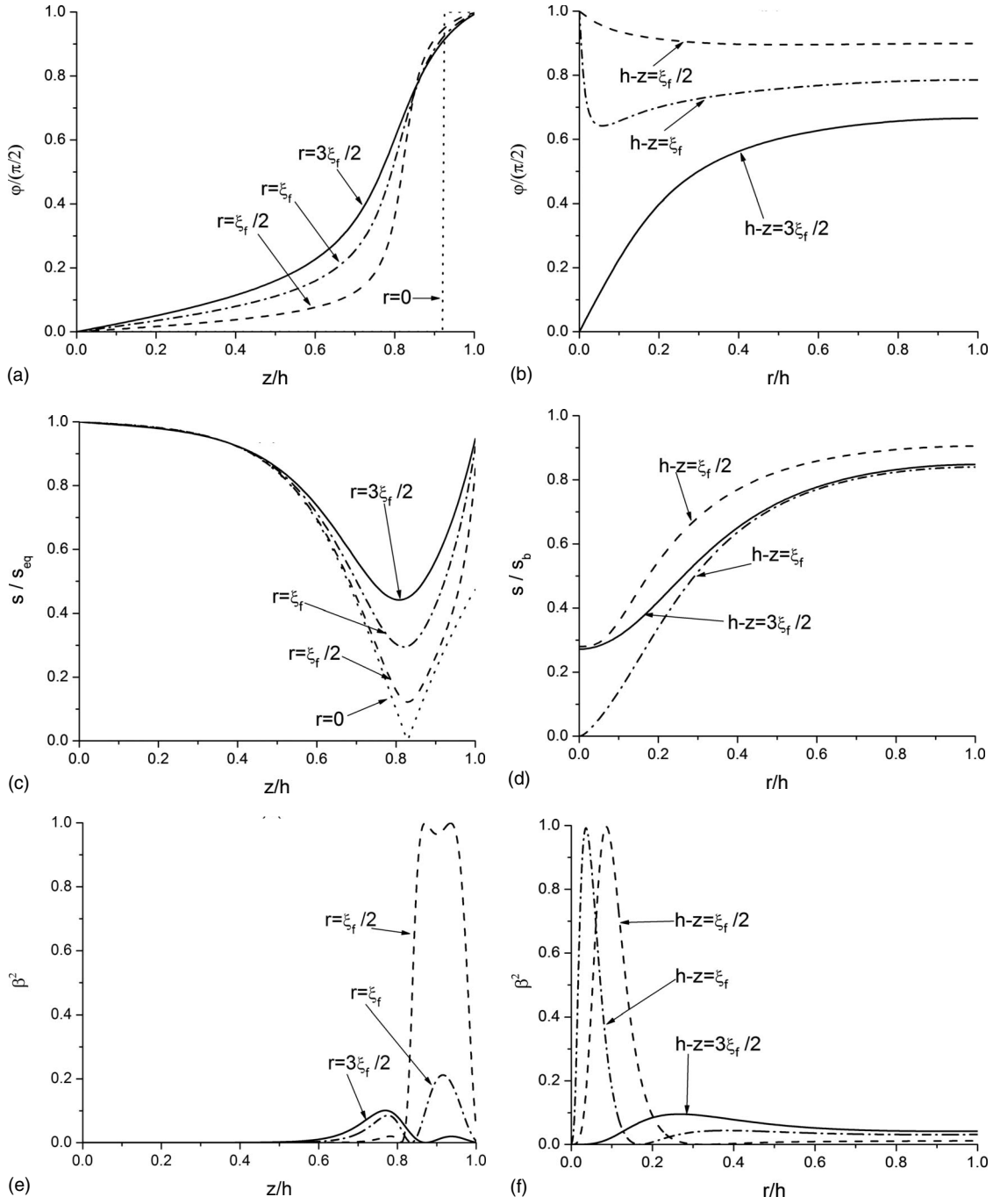

FIG. 7. Representative cross-sections of the boojum structure. Variations along the z axis are in the left panel and those along the r axis are in the right panel. The following cross-sections are shown: (a) $\varphi(r^*,z)$, (b) $\varphi(r,z^*)$, (c) $s(r^*,z)$, (d) $s(r,z^*)$, (e) $\beta^2(r^*,z)$, and (f) $\beta^2(r,z^*)$, where $r^*=\xi_f/2,\xi_f,3\xi_f/2$ and $h-z^*=\xi_f/2,\xi_f,3\xi_f/2$. Moreover, we set throughout $h/\xi_b=10$, $\theta=-8$, $R=h$, and $h/d_e^{(1)}=100$.

exit the cells. In Fig. 11, where $h/\xi_b=4$ and $R/h=0.5$, the critical value $d_c^{(1)}$ of $d_e^{(1)}$ for which $z_{\min}=1$ is given by $d_c^{(1)}\approx 1.5h$.

We also studied the influence of the boundary conditions at $r=R$ on the details of the equilibrium texture. Some representative plots of β^2 for BC$^{(\mathrm{free})}$, BC$^{(\mathrm{rim})}$, and BC$^{(\mathrm{rot})}$ for decreasing h are shown in Figs. 12–14, respectively. We focus attention on OR structures arising when either of the two uniaxial boundary conditions is enforced. A typical pattern for BC$^{(\mathrm{rot})}$, which we label OR$^{(\mathrm{rot})}$, is shown in Fig. 13(f). The canyon surrounded by the ridges with $\beta^2=1$ is in this case closed because of $\beta^2(R,z)=0$. For BC$^{(\mathrm{rim})}$, an additional ring defect is formed at $r=R$ and $z=h$, as shown in Fig. 14(f). We refer to this configuration as the OR$^{(\mathrm{rim})}$. Like the boojum, the ring defect lifts the uniaxial sheet toward the upper plate.

Figures 12–14, further illustrate some stages of the nucleation of the OR structure, when the cell thickness is decreased and when $R\gtrsim\xi_b$ so that finite-size effects are evident. This OR structure develops continuously, as does

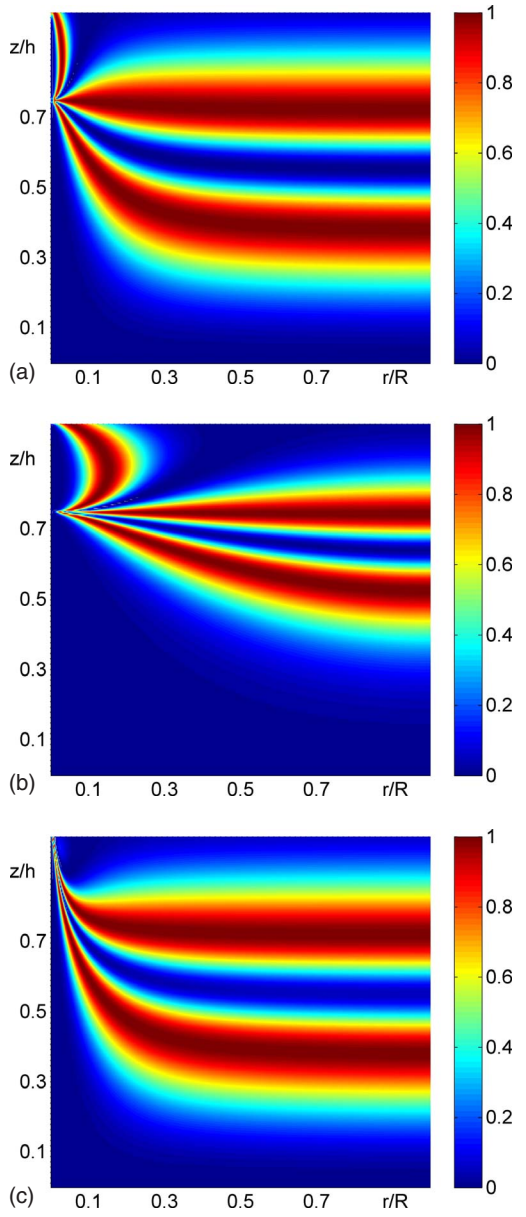

FIG. 8. (Color online) The level curves of $\beta^2(r,z)$ in the OR texture corresponding to the free boundary condition $[\mathrm{BC}^{(\mathrm{free})}]$ at $r=R$. We set $h/\xi_b=2$, $\theta=-8$, $h/d_e^{(1)}=100$. (a) $R/h=5$, (b) $R/h=0.5$, (c) $R/h=5$, and $\mathbf{Q}(0,z)=S_{eq}(\mathbf{e}_z\otimes\mathbf{e}_z-\frac{1}{3}\mathbf{I})$. In all cases, the uniaxial sheet is pinned to the tip of the boojum finger. The color code is the same as in Fig. 6.

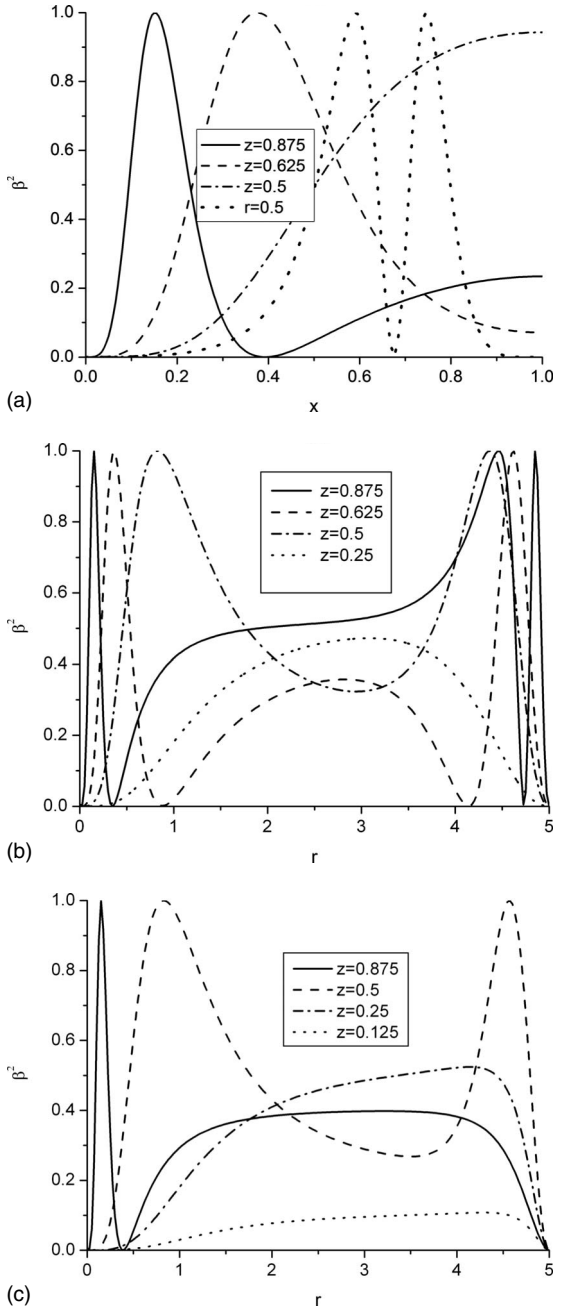

FIG. 9. One dimensional graphs of β^2 at selected values of r or z. (a) $\mathrm{BC}^{(\mathrm{free})}$, $R/h=0.5$, (b) $\mathrm{BC}^{(\mathrm{rim})}$, $R/h=1.5$, (c) $\mathrm{BC}^{(\mathrm{rot})}$, and $R/h=1.5$. For all graphs, $h/d_e^{(1)}=100$ and $\theta=-8$.

$\mathrm{OR}^{(\mathrm{cl})}$. Above a critical thickness $h_c^{(\mathrm{BC})}$, which depends on the boundary condition imposed at $r=R$, the onset of OR can be inferred from the attraction exerted by the defect's core, which for $h>h_c^{(\mathrm{BC})}$ makes the degree of biaxiality larger close to either the boojum or the ring defect. To determine $h_c^{(\mathrm{BC})}$, we decrease gradually h and we record both the local average degree of biaxiality, $\langle\beta^2\rangle_r:=\frac{1}{h}\int_0^h\beta^2(r,z)dz$ at $r=R/2$ and the total average degree of biaxiality $\langle\beta^2\rangle:=\frac{2}{hR^2}\int_0^R\int_0^h\beta^2 rdrdz$. The biaxial defect cores promote the onset of OR and, in fact, both $h_c^{(\mathrm{free})}$ and $h_c^{(\mathrm{rim})}$ increase upon decreasing R. To enrich our analysis we also monitored $\langle\beta^2\rangle_{R/2}$ which reveals changes in the inner biaxial texture.

Figure 15 illustrates how $\langle\beta^2\rangle$ (thick lines) and $\langle\beta^2\rangle_{R/2}$ (thin lines) vary as h is varied. Due to the imposed uniaxial boundary conditions, $\langle\beta^2\rangle<\langle\beta^2\rangle_{R/2}$ for both $\mathrm{OR}^{(\mathrm{rim})}$ and $\mathrm{OR}^{(\mathrm{rot})}$. Conversely, the influence of the boojum on the $\mathrm{OR}^{(\mathrm{free})}$ texture is relatively weak. We found $\langle\beta^2\rangle\sim\langle\beta^2\rangle_{R/2}$ and consequently we plotted only $\langle\beta^2\rangle$ in Fig. 15. Upon decreasing R, $h_c^{(\mathrm{free})}$ slightly increases. On the contrary, the influence of the ring defect can dramatically enhance $h_c^{(\mathrm{rim})}$, as shown in Fig. 16. One sees a large increase in $h_c^{(\mathrm{rim})}$ as R approaches h. In the case of $\mathrm{BC}^{(\mathrm{rot})}$, the "noncritical" character of the essentially uniaxial region at $r=R$ masks the clear onset of the $\mathrm{OR}^{(\mathrm{rot})}$ structure. In this case, the transition

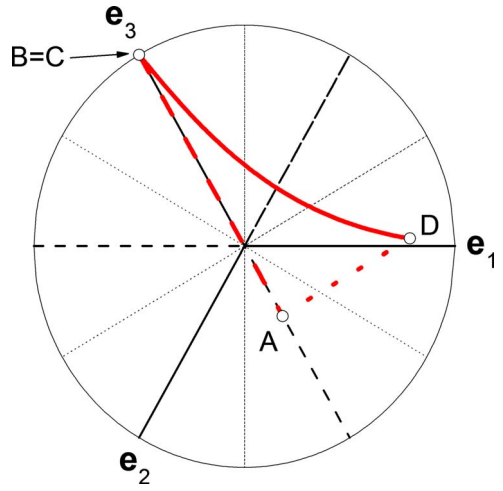

FIG. 10. (Color online) The trajectories in the (s,ψ)-space joining points within the cell for the equilibrium texture shown in Fig. 8(a). In cylindrical coordinates, the relevant points are described by A: $(r=0,\ z=h)$, B: $(r=0,\ z=0)$, C: $(r=R,\ z=0)$, and D: $(r=R,\ z=h)$. The trajectories in real space are straight segments.

between the different competing structures also seems to be gradual.

IV. CONCLUSIONS

We studied equilibrium order textures in nematic liquid crystals confined within a submicrometer hybrid cell. Encouraged by the recent success of mesoscopic approaches [26–28] in predicting the material's behavior in severely confined geometries, we employed the Landau–de Gennes theory in regimes where the geometric and physical length scales are comparable with one another. In particular, we explored the interaction between regions of nonsingular severe elastic distortions and topological defects, along with the structural transitions that could be drastically affected by the presence of topological defects.

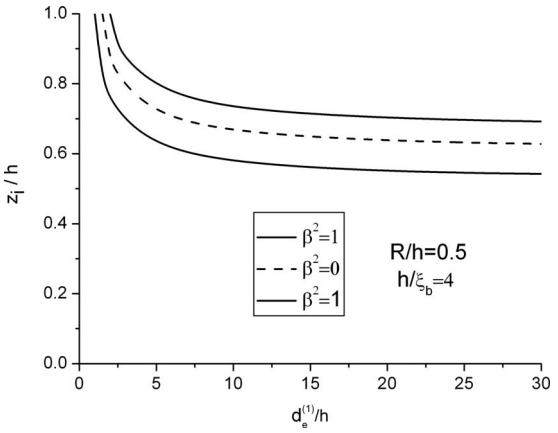

FIG. 11. Evaluation of $(z^{(1)}_{\max}, z_{\min}, z^{(2)}_{\max})$ at $r=R/2$, upon decreasing the anchoring strength $w_1 \propto 1/d_e^{(1)}$ at the upper plate. The OR structure gradually exits the cell. At $z^{(1)}_{\max}$ and $z^{(2)}_{\max}$ the degree of biaxiality β^2 attains its maximum $\beta^2=1$, whereas at $z_{\min}$ it attains its minimum $\beta^2=0$. For strong enough anchoring, the OR is characterized by $0<z^{(1)}_{\max}<z_{\min}<z^{(2)}_{\max}<1$. Here, we chose $\mathrm{BC}^{(\mathrm{free})}$ with $h/\xi_b=4$, $R/h=0.5$, and $\theta=-8$.

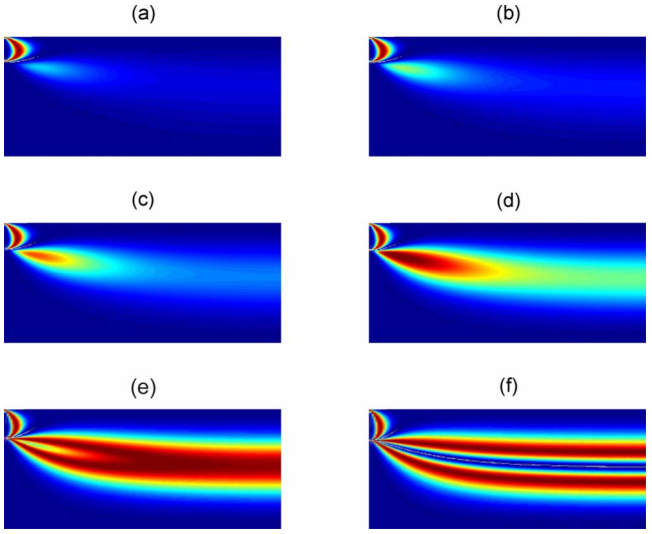

FIG. 12. (Color online) Nucleation of $\mathrm{OR}^{(\mathrm{free})}$ upon decreasing the cell thickness h shown through the level curves of $\beta^2(r,z)$. The scale and the color code are the same as in Fig. 8(a). (a) $h/\xi_b=8$, (b) $h/\xi_b=7.33$, (c) $h/\xi_b=6.67$, (d) $h/\xi_b=6$, (e) $h/\xi_b=5.33$, and (f) $h/\xi_b=4.67$. In all pictures $R/h=1.5$, $h/d_e^{(1)}=100$, and $\theta=-8$. A typical $\mathrm{OR}^{(\mathrm{free})}$ structure is achieved in (f).

Within a cylindrical cell of thickness h and radius R we considered axially symmetric configurations induced by a radial planar anchoring at the upper plate and a homeotropic anchoring at the lower plate, which have the potential to promote topological defects, provided that the anchoring on the upper plate is strong enough. On the lateral surface of the cell, we imposed either free boundary conditions $[\mathrm{BC}^{(\mathrm{free})}]$, or a homogeneous uniaxial alignment along the z axis

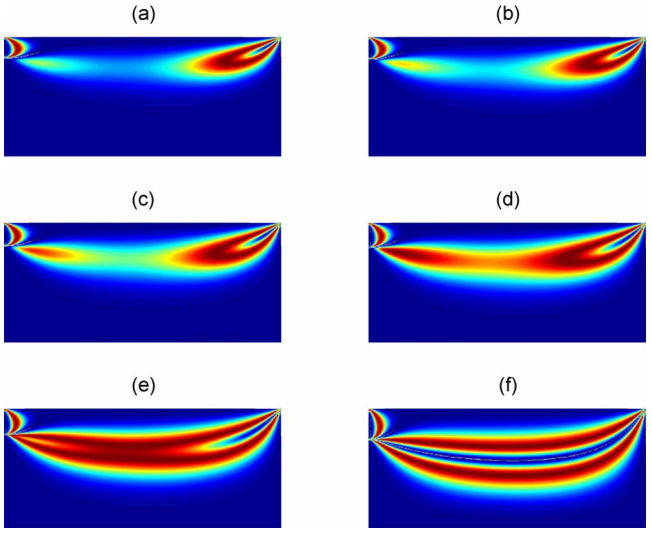

FIG. 13. (Color online) Nucleation of $\mathrm{OR}^{(\mathrm{rim})}$ upon decreasing the cell thickness h, shown through the level curves of $\beta^2(r,z)$. The scale and the color code are the same as in Fig. 8(a). (a) $h/\xi_b=8.67$, (b) $h/\xi_b=8$, (c) $h/\xi_b=7.33$, (d) $h/\xi_b=6.67$, (e) $h/\xi_b=6$, and (f) $h/\xi_b=5.33$. In all pictures $R/h=1.5$, $h/d_e^{(1)}=100$, and $\theta=-8$. A typical $\mathrm{OR}^{(\mathrm{rim})}$ texture is achieved in (f).

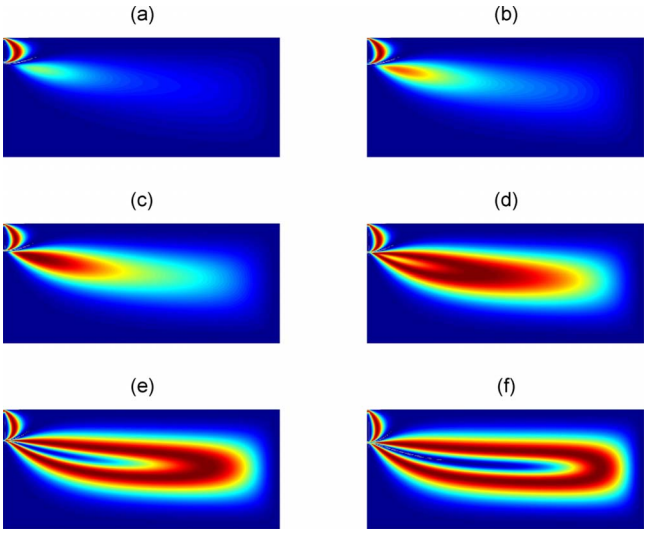

FIG. 14. (Color online) Nucleation of $OR^{(rot)}$ upon decreasing the cell thickness h shown through the level curves of $\beta^2(r,z)$. The scale and the color code are the same as in Fig. 8(a). (a) $h/\xi_b=7.33$, (b) $h/\xi_b=6.67$, (c) $h/\xi_b=6$, (d) $h/\xi_b=5.33$, (e) $h/\xi_b=4.67$, and (f) $h/\xi_b=4$. In all pictures $R/h=1.5$, $h/d_e^{(1)}=100$, and $\theta=-8$. A typical $OR^{(rot)}$ structure is achieved in (f).

$[BC^{(rim)}]$, or a prescribed uniaxial rotation of the nematic director $[BC^{(rot)}]$, all meant to relax or contrast the frustration induced by the boundary conditions on the plates. Besides a boojum, a ring defect also emerges on the upper plate at $r=R$ when $BC^{(rim)}$ is imposed. Values of h and R are set to be larger than, but comparable to the biaxial correlation length ξ_b, that is, where the OR can be stabilized [13,16].

Our study reveals that a negatively (planar) uniaxial sheet, a characteristic feature of OR, can be locally molded by topological defects. In particular, both the boojum and the ring defect attract the uniaxial sheet toward themselves. These effects are even more pronounced for $R\sim h\gtrsim\xi_b$. We also observed that severe elastic distortions virtually abandon the cell upon decreasing the anchoring strength at the upper plate. Furthermore, we demonstrated that a line defect could dramatically increase the critical thickness h_c below which the OR is observed: actually, h_c can be doubled if $h\lesssim R$. This phenomenon has already been observed in [31,36], where structural changes in the nematic equilibrium textures were induced by an applied field. In that case, the critical electric field promoting the onset of OR was approximately decreased by a factor two when a line defect was present in the cell.

Our main concern in this paper was to assess the possible influence of point and line defects on the structural details of OR and on the threshold for its appearance. To enforce a point defect on a plate of a nematic cell, we considered a rather simple surface energy, given by Eq. (7). This raises the question that our conclusions could have been different, had only a different choice for the surface energy been made. We regard Eq. (7) as the prototype of a general family of surface energies enforcing one and the same uniaxial alignment of $\mathbf{Q}$ in the strong anchoring limit. It is shown in Appendix A how to choose the energy strength w in Eq. (7) to approximate a general surface energy density with appropriate growth properties. We believe that the coincidence of the surface minimizers in the strong anchoring limit would make qualitatively similar the ordering textures from both the general and the prototypical surface energies, especially near the strong anchoring limit. Qualitative changes in the structure of the boojum could be obtained by choosing an anisotropic surface interaction energy that promotes with different strengths the orientation of the eigenframe and the degree of ordering of $\mathbf{Q}$. If the latter anchoring strength is much weaker than the former, then the boojum structure would resemble the structure of a half-hedgehog as discussed in detail in [30]. However, here our main objective was to illuminate how defects

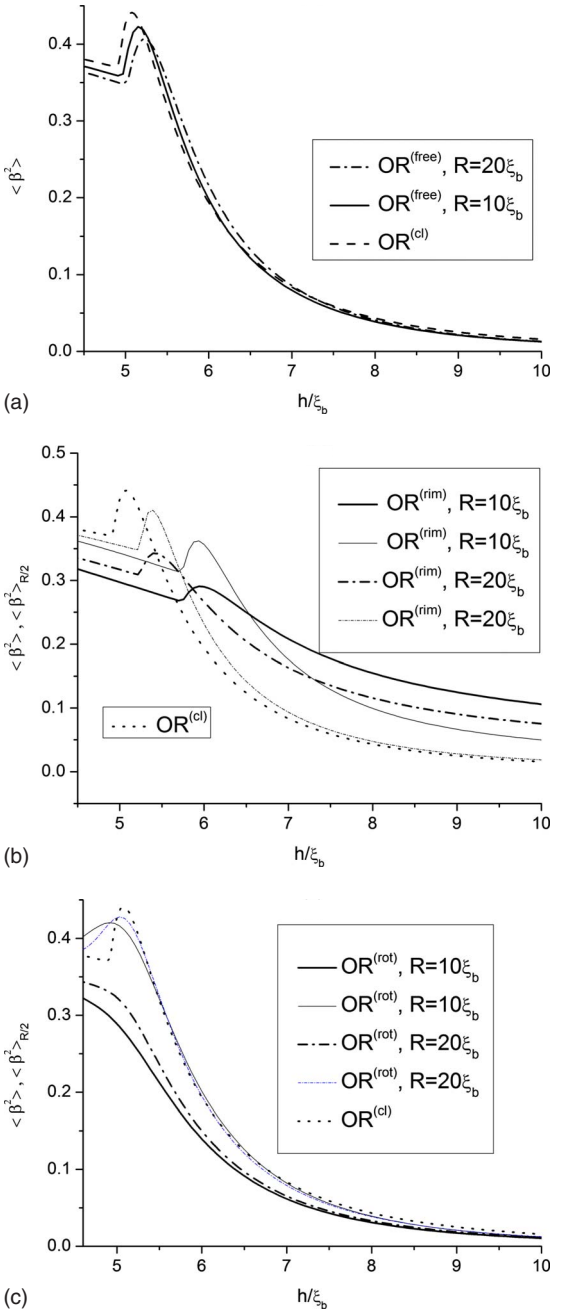

FIG. 15. (Color online) Graphs of $\langle\beta^2\rangle$ (thick lines) and $\langle\beta^2\rangle_{R/2}$ (thin lines) against h for (a) $OR^{(free)}$, (b) $OR^{(rim)}$, and (c) $OR^{(rot)}$. As a reference, we also plot the graph of $\langle\beta^2\rangle$ against h for $OR^{(cl)}$.

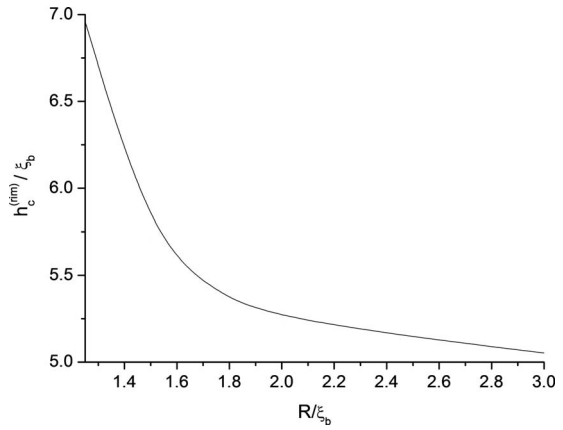

FIG. 16. Dependence of the critical thickness $h_c^{(\mathrm{rim})}$ on R. For $R \sim h_c^{(\mathrm{rim})}$, the presence of the ring defect strongly increases the threshold value $h_c^{(\mathrm{rim})}$.

may alter the OR structure. We showed that both line and point defects—for which we enforced different biaxial core structures by choosing appropriate forms of the surface potential—pin the negatively (planar) uniaxial OR sheet. Therefore, OR textures could be effectively modulated in space via topological defects, with potential use in diverse applications (for example, to establish structures with controlled periodic modulations for photonic crystals [37]). In the absence of defects, the OR uniaxial sheet is placed in the middle of the cell, for equal anchoring strengths at both plates. If defects are introduced, say, at the top plate the whole sheet could be lifted toward this plate. In addition, we found that, at variance with a point defect, a line defect could strongly influence the threshold for the formation of OR textures. Our results suggest that line defects could in general affect strongly phase or structural transitions, where one phase or structure is preferred by the defect core structure, if the characteristic linear size of the region confining the LC sample is comparable to the length of the defect.

APPENDIX A: SURFACE ENERGIES

The surface free-energy density f_s in Eq. (7) was proposed by Nobili and Durand in [38]. When, as in our setting, the tensor $\mathbf{Q}_s$ in Eq. (7) is uniaxial, f_s is a special case of the function

$$f_w := W_{11}\boldsymbol{e}\cdot\mathbf{Q}\boldsymbol{e} + W_{21}\,\mathrm{tr}\,\mathbf{Q}^2 + W_{22}(\boldsymbol{e}\cdot\mathbf{Q}\boldsymbol{e})^2 + W_{23}\mathbf{Q}\boldsymbol{e}\cdot\mathbf{Q}\boldsymbol{e}, \tag{A1}$$

where W_{11}, W_{21}, W_{22}, and W_{23} are material constants. The surface free-energy density f_w is the most general function depending quadratically on the order tensor $\mathbf{Q}$ and on a preferred unit vector $\boldsymbol{e}$, which represents the single local direction of anisotropy of the substrate: $\boldsymbol{e}$ is usually taken to be the unit normal vector $\boldsymbol{\nu}$ to the substrate; for our purposes, however, it is to be identified with the radial unit vector $\boldsymbol{e}_r$. This free-energy density, originally proposed by Poniwierski and Sluckin in [39], can be derived from both a molecular mean-field theory [40,41] and a density functional theory [42]; it has been applied extensively in studying wetting phenomena.

The stationary points of f_w are identified by requiring that

$$\frac{\partial f_w}{\partial \mathbf{Q}} = \mathbf{0}. \tag{A2}$$

It follows from Eq. (A1) that Eq. (A2) reads as

$$W_{11}\overline{\boldsymbol{e}\otimes\boldsymbol{e}} + 2W_{21}\mathbf{Q} + 2W_{22}(\boldsymbol{e}\cdot\mathbf{Q}\boldsymbol{e})\overline{\boldsymbol{e}\otimes\boldsymbol{e}} + 2W_{23}\overline{\mathbf{Q}\boldsymbol{e}\otimes\boldsymbol{e}} = \mathbf{0}, \tag{A3}$$

where $\overline{\mathbf{A}}$ denotes the symmetric, traceless part of the second-rank tensor $\mathbf{A}$. As also remarked in [43], if $W_{21}=0$, the solution to Eq. (A3) is degenerate, as it is given by any tensor $\mathbf{Q}_0$ for which $\boldsymbol{e}$ is an eigenvector:

$$\mathbf{Q}_0\boldsymbol{e} = \lambda\boldsymbol{e},$$

where

$$\lambda = -\frac{W_{11}}{2(W_{22}+W_{23})}.$$

For such a tensor to comply with its statistical interpretation, λ must be bound to the interval $[-\frac{1}{3},\frac{2}{3}]$. If $W_{21}\neq 0$, the only solution of Eq. (A3) is

$$\mathbf{Q}_0 = \mu\overline{\boldsymbol{e}\otimes\boldsymbol{e}}, \tag{A4}$$

where

$$\mu = -\frac{3}{2}\frac{W_{11}}{3W_{21}+2(W_{22}+W_{23})} \in \left[-\frac{1}{2},1\right].$$

With $\mathbf{Q}_0$ as in Eq. (A4), to within an inessential additive constant, f_w reduces to

$$f_s = \frac{1}{2}w\,\mathrm{tr}(\mathbf{Q}-\mathbf{Q}_0)^2, \tag{A5}$$

provided that

$$W_{11} = -\mu w, \quad W_{21} = \frac{1}{2}w, \quad W_{22} = W_{23} = 0. \tag{A6}$$

$\mathbf{Q}_0$ in Eq. (A4) is an isolated minimizer of f_w whenever the fourth-rank tensor

$$\mathbb{S} := \frac{\partial^2 f_w}{\partial \mathbf{Q}^2}$$

is positive definite. By differentiating in $\mathbf{Q}$ the left-hand side of Eq. (A3), one arrives at

$$\mathbb{S} = 2(W_{21}\mathbb{I} + W_{22}\overline{\boldsymbol{e}\otimes\boldsymbol{e}}\otimes\overline{\boldsymbol{e}\otimes\boldsymbol{e}} + W_{23}\mathbb{E}), \tag{A7}$$

where $\mathbb{I}$ is the identity on the five-dimensional linear space $\mathcal{U}$ of all symmetric, traceless second-order tensors, and $\mathbb{E}$ is the linear mapping onto $\mathcal{U}$ defined by

$$\mathbb{E}[\mathbf{U}] := \overline{\mathbf{U}\boldsymbol{e}\otimes\boldsymbol{e}} \quad \text{for all} \quad \mathbf{U}\in\mathcal{U}.$$

$\mathbb{E}$ is a symmetric forth-rank tensor onto $\mathcal{U}$; its *eigentensors* $\mathbf{b}$ are members of $\mathcal{U}$ that satisfy the equation

$$\overline{\mathbf{b}\boldsymbol{e}\otimes\boldsymbol{e}} = \alpha\mathbf{b} \tag{A8}$$

with α real. It is easily seen that

$$\mathbf{b} = \overline{\boldsymbol{e}\otimes\boldsymbol{e}}$$

is a solution of Eq. (A8) with $\alpha=\frac{2}{3}$. Then the other eigentensors of $\mathbb{E}$ are orthogonal to

$$\overline{\boldsymbol{e}\otimes\boldsymbol{e}},$$

and so they satisfy

$$\boldsymbol{e}\cdot\mathbf{b}\boldsymbol{e} = 0. \tag{A9}$$

By applying both sides of Eq. (A8) to $\boldsymbol{e}$, making use of Eq. (A9), we obtain

$$\frac{1}{2}\mathbf{b}\boldsymbol{e} = \alpha\mathbf{b}\boldsymbol{e},$$

whence it follows that either $\mathbf{b}\boldsymbol{e}=\mathbf{0}$ or $\alpha=\frac{1}{2}$. In the former case, again by Eq. (A8), $\alpha=0$. We thus conclude that the eigenvalues of $\mathbb{E}$ are $\frac{2}{3}$, $\frac{1}{2}$, and 0. While the eigenspace $\mathcal{U}_{2/3}$ corresponding to the first eigenvalue has dimension 1, both eigenspaces $\mathcal{U}_{1/2}$ and $\mathcal{U}_0$ corresponding to the other eigenvalues have dimension 2. It can be easily proved that $\mathcal{U}_{1/2}$ is generated by the tensors $(\boldsymbol{e}\otimes\boldsymbol{e}_\perp+\boldsymbol{e}_\perp\otimes\boldsymbol{e})$ and $(\boldsymbol{e}\otimes\boldsymbol{e}'_\perp+\boldsymbol{e}'_\perp\otimes\boldsymbol{e})$, where both $\boldsymbol{e}_\perp$ and $\boldsymbol{e}'_\perp$ are unit vectors orthogonal to $\boldsymbol{e}$ and to each other. Similarly, $\mathcal{U}_0$ is generated by the tensors $(\boldsymbol{e}_\perp\otimes\boldsymbol{e}'_\perp+\boldsymbol{e}'_\perp\otimes\boldsymbol{e}_\perp)$ and $(\boldsymbol{e}_\perp\otimes\boldsymbol{e}_\perp-\boldsymbol{e}'_\perp\otimes\boldsymbol{e}'_\perp)$. $\mathcal{U}_{2/3}$, $\mathcal{U}_{1/2}$, and $\mathcal{U}_0$ are also the eigenspaces of $\mathbb{S}$, with corresponding eigenvalues

$$\sigma_{2/3} = 2\left(W_{21}+\frac{2}{3}W_{22}+\frac{2}{3}W_{23}\right),$$

$$\sigma_{1/2} = 2W_{21}+W_{23},$$

$$\sigma_0 = 2W_{21}.$$

Thus, $\mathbb{S}$ is positive definite, whenever $\sigma_{2/3}$, $\sigma_{1/2}$, and σ_0 are all positive; in such a case, $\mathbf{Q}_0$ in Eq. (A4) is the absolute minimizer of f_w and it represents the preferred ordered state on the surface.

Even when Eqs. (A6) are not satisfied, and so f_w and f_s do not coincide, we may determine w in Eq. (A5) so as to make f_s the closest approximation to f_w, when both have the same minimizer $\mathbf{Q}_0$ as in Eq. (A4). In the light of the above stability analysis, w can be determined by requiring that the forth-rank tensor

$$\mathbb{S}' = \frac{\partial^2 f_s}{\partial\mathbf{Q}^2} = w\mathbb{I}$$

be the closest to $\mathbb{S}$ in the tensor norm. Thus, we determine w by requiring that

$$|\mathbb{S}-\mathbb{S}'|^2 = \left[2\left(W_{21}+\frac{2}{3}W_{22}+\frac{2}{3}W_{23}\right)-w\right]^2 + 2(2W_{21}+W_{23}-w)^2+2(2W_{21}-w)^2.$$

An easy computation gives

$$w = \frac{2}{15}(15W_{21}+2W_{22}+5W_{23}).$$

Inserting this value of w in Eq. (A5) delivers the function f_s that best approximates f_w.

Modified versions of Eq. (A1) have also been introduced to model substrates with more than a single direction of anisotropy. For example, in [43,44], the following surface free-energy density f_a has been proposed, later also applied in [45]:

$$f_a := -w_a\,\mathrm{tr}(\mathbf{Q}\mathbf{H}), \tag{A10}$$

where $\mathbf{H}$ is a symmetric traceless second-rank tensor that mimics the local properties of the substrate. In this model, the surface free-energy density is linear in $\mathbf{Q}$, and so it can be minimized only by enforcing in an extrinsic, artificial fashion the bounds on $\mathbf{Q}$ that justify its statistical interpretation. However, as shown in [46] in the limit of strong anchoring, there is no guarantee that these bounds are obeyed even in bulk, where the Landau–de Gennes potential favors a definite uniaxial state. Care must in general be used when employing a surface energy density unbounded from below like Eq. (A10), to avoid the occurrence of a boundary layer where the order tensor field minimizing the total free-energy functional violates the statistical bounds. An expression for f_a more appropriate than Eq. (A10) would be a quadratic function in $\mathbf{Q}$, also depending on $\mathbf{H}$, which attains an isolated minimum as f_w in Eq. (A1).

APPENDIX B: EQUILIBRIUM EQUATIONS

To minimize the rescaled free-energy functional

$$\mathcal{F}[\mathbf{Q}] = \int_0^1 dz\int_0^R [f_e(\mathbf{Q})+f_c(\mathbf{Q})]rdr + \int_0^R f_s(\mathbf{Q},\mathbf{Q}_s)rdr \tag{B1}$$

in the class of symmetric, traceless tensors $\mathbf{Q}$ represented by Eq. (9), we first compute the third-rank tensor $\nabla\mathbf{Q}$. Resorting to components, we observe that $\mathbf{Q}$ has the following structure:

$$Q_{kh} = q^\alpha e^\alpha_k e^\alpha_h,$$

where $\alpha=0,1,2$, $\boldsymbol{e}^0:=\boldsymbol{e}_\vartheta$, $\boldsymbol{e}^1:=\boldsymbol{e}_r$, $\boldsymbol{e}^2:=\boldsymbol{e}_z$, and summation over the index α is understood. We then note that

$$Q_{kh,i} = q^\alpha_{,i}e^\alpha_k e^\alpha_h + q^\alpha e^\alpha_{k,i}e^\alpha_h + q^\alpha e^\alpha_k e^\alpha_{h,i}$$

and that the gradients $e^\alpha_{k,i}$ are diadic products, so that $e^\alpha_{k,i}=a^\alpha_k b^\alpha_i$. By use of

$$\nabla\boldsymbol{e}_r = \frac{1}{r}\boldsymbol{e}_\vartheta\otimes\boldsymbol{e}_\vartheta, \quad \nabla\boldsymbol{e}_\vartheta = -\frac{1}{r}\boldsymbol{e}_r\otimes\boldsymbol{e}_\vartheta, \quad \text{and} \quad \nabla\boldsymbol{e}_z = \mathbf{0}$$

(see, e.g., p. 77 of [8]) and by reverting to intrinsic notation, we arrive at

$$\nabla \mathbf{Q} = -2\boldsymbol{e}_\vartheta \otimes \boldsymbol{e}_\vartheta \otimes \nabla q_0 + \boldsymbol{e}_r \otimes \boldsymbol{e}_r \otimes \nabla(q_0 + q_\delta) + \boldsymbol{e}_z \otimes \boldsymbol{e}_z \otimes \nabla(q_0 - q_\delta) + \frac{2q_0}{r}(\boldsymbol{e}_r \otimes \boldsymbol{e}_\vartheta \otimes \boldsymbol{e}_\vartheta + \boldsymbol{e}_\vartheta \otimes \boldsymbol{e}_r \otimes \boldsymbol{e}_\vartheta) + (\boldsymbol{e}_r \otimes \boldsymbol{e}_z \otimes \nabla q_m + \boldsymbol{e}_z \otimes \boldsymbol{e}_r \otimes \nabla q_m) + \frac{q_m}{r}(\boldsymbol{e}_\vartheta \otimes \boldsymbol{e}_z \otimes \boldsymbol{e}_\vartheta + \boldsymbol{e}_z \otimes \boldsymbol{e}_\vartheta \otimes \boldsymbol{e}_\vartheta) + \frac{q_0 + q_\delta}{r}(\boldsymbol{e}_\vartheta \otimes \boldsymbol{e}_r \otimes \boldsymbol{e}_\vartheta + \boldsymbol{e}_r \otimes \boldsymbol{e}_\vartheta \otimes \boldsymbol{e}_\vartheta). \tag{B2}$$

Applying a standard method, we change $\mathbf{Q}$ into a perturbed tensor $\mathbf{Q}_\varepsilon$ by altering q_0, q_δ, and q_m in Eq. (9) as below

$$q_0^\varepsilon := q_0 + \varepsilon u_1, \tag{B3a}$$

$$q_\delta^\varepsilon := q_\delta + \varepsilon u_2, \tag{B3b}$$

$$q_m^\varepsilon := q_m + \varepsilon u_3, \tag{B3c}$$

where u_1, u_2, and u_3 are the three smooth arbitrary functions of r and z. We then expand $\mathcal{F}[\mathbf{Q}_\varepsilon]$ in ε retaining only the first-order terms; the first variation of $\mathcal{F}$ is defined as

$$\delta\mathcal{F}(\mathbf{Q})[u,h,v] = \left.\frac{d\mathcal{F}[\mathbf{Q}_\varepsilon]}{d\varepsilon}\right|_{\varepsilon=0}.$$

By Eq. (B2), we obtain

$$|\nabla \mathbf{Q}|^2 = 2\left\{[3|\nabla q_0|^2 + |\nabla q_\delta|^2 + |\nabla q_m|^2] + \frac{1}{r^2}[q_m^2 + (3q_0 + q_\delta)^2]\right\} \tag{B4}$$

and one can easily check that

$$\mathrm{tr}\,\mathbf{Q}^2 = 2(q_m^2 + q_\delta^2 + 3q_0^2) \tag{B5}$$

and

$$\mathrm{tr}\,\mathbf{Q}^3 = 6q_0(q_\delta^2 + q_m^2 - q_0^2). \tag{B6}$$

By inserting Eqs. (B4)–(B6) into $\mathcal{F}$, after several integrations by parts, we give $\delta\mathcal{F}$ the following expression:

$$\begin{aligned}\delta\mathcal{F}[u_1,u_2,u_3] = {} & 2\left(\frac{\xi_b^{(0)}}{h}\right)^2 \int_0^1\int_0^R r\left[\frac{1}{r^2}(3(3q_0+q_\delta)u_1 + (3q_0+q_\delta)u_2 + q_m u_3) - (3u_1\Delta q_0 + u_2\Delta q_\delta + u_3\Delta q_m)\right]drdz \\ & + \int_0^1\int_0^R r\{2A(3q_0u_1 + q_\delta u_2 + q_m u_3) - 2B[2(q_\delta u_2 + q_m u_3 - q_0 u_1) + u_1(q_m^2 + q_\delta^2 - q_0^2)] \\ & + 4C(q_m^2 + q_\delta^2 + 3q_0^2)(3q_0u_1 + q_\delta u_2 + q_m u_3)\}drdz + 2\left(\frac{\xi_b^{(0)}}{h}\right)^2 \int_0^R r[3u_1 q_{0,z}(r,1) + u_2 q_{\delta,z}(r,1) + u_3 q_{m,z}(r,1)]dr \\ & + 2\frac{(\xi_b^{(0)})^2}{h d_e^{(1)}}\int_0^R r(3q_0u_1 + q_\delta u_2 + q_m u_3)dr - \left(\frac{(\xi_b^{(0)})^2}{h d_e^{(1)}}\right)^2 \int_0^R r[-2u_1 q_{\vartheta\vartheta}^s + (u_1+u_2)q_{rr}^s + (u_1-u_2)q_{zz}^s + 2u_3 q_{rz}^s]dr \\ & + 2\left(\frac{\xi_b^{(0)}}{h}\right)^2 \int_0^1 [3u_1 q_{0,r}(R,z) + u_2 q_{\delta,r}(R,z) + u_3 q_{m,r}(R,z)]dz, \end{aligned} \tag{B7}$$

where the preferred order tensor $\mathbf{Q}_s$ at $z=1$ was written as

$$\mathbf{Q}_s = q_{rr}^s \boldsymbol{e}_r \otimes \boldsymbol{e}_r + q_{zz}^s \boldsymbol{e}_z \otimes \boldsymbol{e}_z + q_{\vartheta\vartheta}^s \boldsymbol{e}_\vartheta \otimes \boldsymbol{e}_\vartheta + q_{rz}^s(\boldsymbol{e}_r \otimes \boldsymbol{e}_z + \boldsymbol{e}_z \otimes \boldsymbol{e}_r) + \mathbf{Q}_n$$

with $\mathbf{Q}_n$ a tensor that does not contribute to the first variation in the surface free-energy, in view of the representation assumed for $\mathbf{Q}$ in Eq. (9). By recalling the expression of the Laplace operator in cylindrical coordinates, we readily arrive at the equilibrium equations (26)–(28) in the main text from requiring $\delta\mathcal{F}$ in Eq. (B7) to vanish identically for all u_1, u_2, and u_3.

[1] I. Muševič, K. Kočevar, and U. Kržič, Rev. Sci. Instrum. **76**, 043701 (2005).
[2] J. Scott, Science **315**, 954 (2007).
[3] G. Atwood, Science **321**, 210 (2008).
[4] M. Kleman and O. D. Lavrentovich, *Soft Matter Physics* (Springer, Berlin, 2002).
[5] F. R. Hung, O. Guzman, B. T. Gettelfinger, N. L. Abbott, and J. J. de Pablo, Phys. Rev. E **74**, 011711 (2006).
[6] W. H. Zurek, Nature (London) **317**, 505 (1985).
[7] P. Palffy-Muhoray, Phys. Today **60**(9), 54 (2007).
[8] E. G. Virga, *Variational Theories for Liquid Crystals* (Chapman Hall, London, 1994).
[9] T. Kibble, Phys. Today **60**(9), 47 (2007).
[10] N. Mermin, Rev. Mod. Phys. **51**, 591 (1979).
[11] S. Kralj and E. G. Virga, J. Phys. A **34**, 829 (2001).
[12] P. G. de Gennes and J. Prost, *The Physics of Liquid Crystals* (Oxford University Press, Oxford, 1993).
[13] P. Palffy-Muhoray, E. C. Gartland, and J. R. Kelly, Liq. Cryst. **16**, 713 (1994).
[14] R. Barberi, F. Ciuchi, G. Durand, M. Iovane, D. Sikharulidze, A. Sonnet, and E. Virga, Eur. Phys. J. E **13**, 61 (2004).
[15] F. Bisi, E. C. Gartland, R. Rosso, and E. G. Virga, Phys. Rev. E **68**, 021707 (2003).
[16] F. Bisi, E. G. Virga, and G. E. Durand, Phys. Rev. E **70**, 042701 (2004).
[17] M. Ambrožič, F. Bisi, and E. G. Virga, Continuum Mech. Thermodyn. **20**, 193 (2008).
[18] N. Schopohl and T. J. Sluckin, Phys. Rev. Lett. **59**, 2582 (1987).
[19] R. Rosso and E. G. Virga, J. Phys. A **29**, 4247 (1996).
[20] S. Kralj, E. G. Virga, and S. Žumer, Phys. Rev. E **60**, 1858 (1999).
[21] G. De Luca and A. D. Rey, J. Chem. Phys. **127**, 104902 (2007).
[22] B. M. Wincure and A. D. Rey, Nano Lett. **7**, 1474 (2007).
[23] C. Zhou, P. Yue, and J. Feng, Langmuir **24**, 3099 (2008).
[24] O. Guzman, E. B. Kim, S. Grollau, N. L. Abbott, and J. J. de Pablo, Phys. Rev. Lett. **91**, 235507 (2003).
[25] E. Kim, O. Guzman, S. Grollau, N. Abbot, and J. de Pablo, J. Chem. Phys. **121**, 1949 (2004).
[26] K. Kočevar and I. Muševič, Phys. Rev. E **65**, 021703 (2002).
[27] S. Kralj, G. Cordoyiannis, A. Zidanšek, G. Lahajnar, H. Amenitsch, S. Žumer, and Z. Kutnjak, J. Chem. Phys. **127**, 154905 (2007).
[28] A. V. Kityk, M. Wolff, K. Knorr, D. Morineau, R. Lefort, and P. Huber, Phys. Rev. Lett. **101**, 187801 (2008).
[29] P. Kaiser, W. Wiese, and S. Hess, J. Non-Equilib. Thermodyn. **17**, 153 (1992).
[30] S. Kralj, R. Rosso, and E. G. Virga, Phys. Rev. E **78**, 031701 (2008).
[31] M. Ambrožič, S. Kralj, and E. G. Virga, Phys. Rev. E **75**, 031708 (2007).
[32] B. Zappone, P. Richetti, R. Barberi, R. Bartolino, and H. T. Nguyen, Phys. Rev. E **71**, 041703 (2005).
[33] W. H. Press, B. P. Flannery, S. A. Teukolsky, and W. Vetterling, *Numerical Recipies* (Cambridge University Press, Cambridge, England, 1986).
[34] D. Svenšek and S. Žumer, Phys. Rev. E **66**, 021712 (2002).
[35] I. Muševič, M. Škarabot, U. Tkalec, M. Ravnik, and S. Žumer, Science **313**, 954 (2006).
[36] G. Lombardo, H. Ayeb, F. Ciuchi, M. P. DeSanto, R. Barberi, R. Bartolino, E. G. Virga, and G. E. Durand, Phys. Rev. E **77**, 020702(R) (2008).
[37] H. Kikuchi, M. Yokota, Y. Hisakado, H. Yang, and T. Kajiyama, Nature Mater. **1**, 64 (2002).
[38] M. Nobili and G. Durand, Phys. Rev. A **46**, R6174 (1992).
[39] T. Sluckin and A. Poniwierski, in *Fluid Interfacial Phenomena*, edited by C. Croxton (Wiley, Chichister, 1986), pp. 215–253.
[40] A. K. Sen and D. E. Sullivan, Phys. Rev. A **35**, 1391 (1987).
[41] J.-B. Fournier and P. Galatola, EPL **72**, 403 (2005).
[42] M. A. Osipov and S. Hess, J. Chem. Phys. **99**, 4181 (1993).
[43] A. Poniwierski and A. Samborski, Liq. Cryst. **27**, 1285 (2000).
[44] A. Poniewierski and A. Samborski, Pol. J. Chem. **75**, 463 (2001).
[45] C. Tsakonas, A. Davidson, C. Brown, and J. Mottram, Appl. Phys. Lett. **90**, 111913 (2007).
[46] A. Majumdar, e-print arXiv:0808.1870.